PAPER • OPEN ACCESS

Few quantum walkers for the generation of vortex creep on bosonic flux ladders

View the article online for updates and enhancements.

New Journal of Physics

The open access journal at the forefront of physics

CrossMark

PAPER

Few quantum walkers for the generation of vortex creep on bosonic flux ladders

Weijie Huang[1] and Yao Yao[1,2,*]

[1] Department of Physics, South China University of Technology, Guangzhou 510640, People's Republic of China
[2] State Key Laboratory of Luminescent Materials and Devices, South China University of Technology, Guangzhou 510640, People's Republic of China
[*] Author to whom any correspondence should be addressed.

E-mail: yaoyao2016@scut.edu.cn

Abstract

We investigate the quantum–classical correspondence of vortex creep within the framework of quantum ladder lattice with artificial gauge. By introducing operators to characterize microscopic vortices in the bosonic flux ladder, we focus on quantum walks initiated from states with one, two and four particles localized at the central sites of the ladder. In the single-particle systems, we observe an asymmetric spreading of vortices stemming from the specific construction of the initial states and the gauge choice. In the two- and four-particle systems, comparisons across different conditions reveal that the individual application of flux and interactions slows down particle propagation due to pairing and vortex formation. Notably, when both flux and interaction are present concurrently, our results demonstrate that the mean square displacement (MSD) of the vortices grows significantly slower than the typical MSD $\sim t^2$ for quantum walk, instead approaching the characteristic behavior of classical walk MSD $\sim t$. This indicates that the observed spreading process is consistent with the classical walk of vortices formed by circulating particles, i.e. vortex creep in superconductors.

1. Introduction

At sufficiently high magnetic fields, vortices emerge inside the type-II superconductors due to the penetration of magnetic flux composed of circulating supercurrents [1]. These vortices are often regarded as macroscopic structures in the study of superconductors [2], and their dynamics have attracted significant attention due to their fundamental importance and practical applications [3]. In the profoundly influential classical vortex creep models, these vortices are set in motion by current-induced forces and thermal energy, constituting a major source of dissipation in superconductors [4]. Researchers have also made substantial progress in extending the quantum description of vortex creep and developed the quantum collective creep theory within the framework of macroscopic quantum tunneling (MQT) [5–7], despite facing certain challenges. Currently, there exists a wealth of research exploring the behavior of vortices in superconducting materials, yet the understanding remains limited due to the complexity of vortex systems [2, 8–10].

Simulating vortex creep with quantum dynamics on lattice models presents an innovative and intriguing avenue of research, providing valuable insights into the behavior of vortices in superconductors. The bosonic flux-ladder model offers a promising platform supported by advanced experimental realizations in various systems [11–16] and sophisticated theoretical methods [17–28]. The two-leg bosonic flux ladder hosts a variety of emergent quantum phases under the influence of on-site interactions and magnetic fields [17–21, 28–35]. Notably, it exhibits the Meissner and vortex phases which are reminiscent of those in type-II superconductors [17, 20, 22]. The Meissner phase is characterized by a finite, uniform chiral leg current circulating the ladder, while the rung current vanishes. In the vortex phase, rung currents develop on the inner rungs, forming vortices that suppress the chiral current.

Recent studies have explored the quantum dynamics of interacting bosons on flux ladders [11–16, 27, 28, 36–38]. Particularly, the analysis of reentrant dynamics in the quantum walk of interacting bosons [37] have suggested that the vortices in the ladder have an impact on these processes. However, the motion of vortices in this context has received less attention, and the analysis from the vortex perspective remains a challenging aspect to explore. The difficulties arise from two aspects. On one hand, the effects of interactions and flux have already resulted in rich and complex dynamics in the two-particle systems, including chiral dynamics [13, 36], reentrant behaviors [37, 38], and various forms of particle pairings [39–42]. On the other hand, the motion of vortices in the flux ladder remains difficult to identify and quantify [20, 21, 31, 32], with the potential complexity arising from possible vortex-vortex interactions.

The quantum walk of interacting particles can differ significantly due to their sensitivity to particle statistics [40–44], external gauge fields [13, 36–38, 45–47], inter-particle interactions [42, 43], disorder [48, 49], and topology in lattice systems [50, 51]. Notably, the dynamics of two-particle states influenced by uniform flux, on-site interaction strength, and rung-to-leg hopping ratio have been systematically studied in references [37–39], focusing primarily on radial and chiral particle motion. Additionally, The choice of initial states plays a crucial role [13, 36–38]. When considering on-site interaction, two bosons initially located at the same site or adjacent sites on the same leg can form an on-site bound pair [40–42], leading to slower dynamics. Alternatively, two bosons initially located on adjacent sites of the same rung can form a rung-localized pair [39].

In this work, we focus on the propagation of vortices during the quantum walk on the interacting flux-ladder model [13, 36–38]. Our study is motivated by the exploration of vortex dynamics in quantum flux ladder systems, aiming to provide novel insights into the quantum-to-classical transition in vortex behavior. We introduce new dimeric operators and the vortex angular momentum to characterize the vortices. Key determinants of the systems include the construction of initial states, on-site interactions, and uniform magnetic flux. The interaction-induced pairing and the formation of vortices both contribute to particle localization. Meanwhile, the motion of these vortices, driven by particle hopping, competes with the localization effects. This interplay can lead to a transition in vortex behavior from quantum to classical, analogous to the vortex creep phenomenon. This transition is similar to the quantum-to-classical transition observed in charge transport in organic semiconductors [52–54], where dynamic disorder induces localization.

Specifically, we calculate the time evolution of the operators in the quantum walk across different system configurations. Starting from single-particle localized states, we study the impact of the gauge choice and initial state construction on single-particle dynamics, which leads to asymmetry spreading. Subsequently, we extend our research to two-particle systems and four-particle systems to investigate the vortex propagation under the influence of both uniform magnetic fields and on-site interaction. The particle pairing induced by interaction and the formation of vortices induced by flux significantly coexist and facilitate with each other and remarkably influence the dynamics. By comparing the results across different conditions, we analyze the individual and combined effects of the uniform magnetic fields and interaction. Both the magnetic field and interaction suppress the particle spreading, and when combined, they induce a transition from quantum ballistic behavior to classical diffusion behavior, as indicated by the mean square displacement (MSD), illustrating vortex creep.

This paper is organized as follows. In section 2, we briefly introduce the model in two different gauge conventions as well as some key observables. In section 3, we provide the main results of one-, two- and four-particle systems. Section 4 presents the summary of our work.
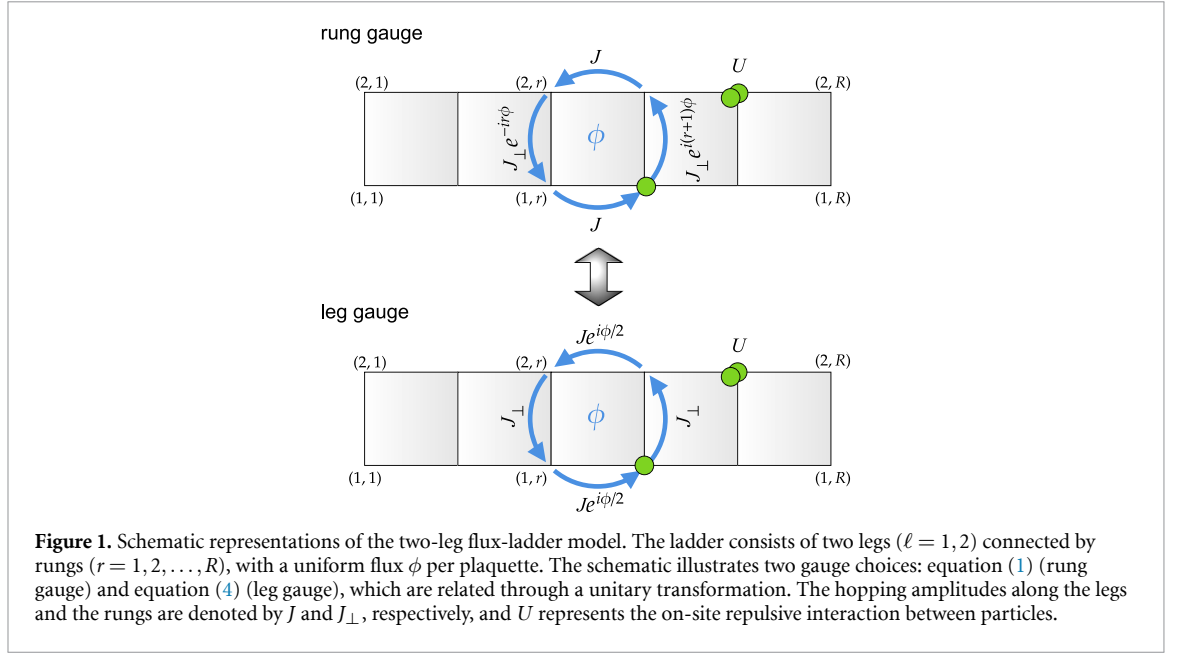
2. Model

2.1. Hamiltonian
The Hamiltonian of a paradigmatic two-leg flux-ladder model [17] (see figure 1) is given by

$$H_0 = -J\sum_{r=1}^{R-1}\sum_{\ell=1}^{2}\left(c_{\ell,r+1}^\dagger c_{\ell,r} + \text{H.c.}\right) - J_\perp \sum_{r=1}^{R}\left(e^{-ir\phi}c_{1,r}^\dagger c_{2,r} + \text{H.c.}\right), \tag{1}$$

$$H_U = \frac{U}{2}\sum_{r=1}^{R}\sum_{\ell=1}^{2}n_{\ell,r}\left(n_{\ell,r}-1\right), \tag{2}$$

where total Hamiltonian is $H = H_0 + H_U$, describing a ladder with R rungs. Herein, J and $J_\perp$ are the hoping amplitude along the legs (labeled by $\ell = 1, 2$), and the rungs (labeled by $r = 1, 2, \ldots, R$) of the ladder. The local operator $c_{\ell,r}^\dagger(c_{\ell,r})$ creates (annihilates) a boson on the site (ℓ, r) and $n_{\ell,r} = c_{\ell,r}^\dagger c_{\ell,r}$ is the corresponding particle number operator. The flux introduces Peierls phase factors in the hopping terms, giving the wave

Figure 1. Schematic representations of the two-leg flux-ladder model. The ladder consists of two legs ($\ell = 1, 2$) connected by rungs ($r = 1, 2, \ldots, R$), with a uniform flux ϕ per plaquette. The schematic illustrates two gauge choices: equation (1) (rung gauge) and equation (4) (leg gauge), which are related through a unitary transformation. The hopping amplitudes along the legs and the rungs are denoted by J and $J_\perp$, respectively, and U represents the on-site repulsive interaction between particles.

function a phase $e^{\pm i \phi}$ when a particle encircles a plaquette, with the sign determined by the circulation direction. U is the on-site repulsive interaction that influences both quantum walk dynamics and ground state properties. Throughout this work, we set lattice constant $a = 1$, $\hbar = 1$. In order to be easy to identify the propagating vortex, we consider the Hamiltonian $H = H_0 + H_U$ with $\phi = 0.7\pi$, $J = 1$, $J_\perp = 2$, $U = 2$, $R = 60$, with which the ground state is in the vortex-liquid superfluids (V-SF) phase [21] hosting delocalized vortices (see the next subsection for more details of the ground states).

It is worth noting that, the model possesses a gauge freedom such that one can choose different Peierls phase factors as long as the total flux of a single ladder plaquette remains invariant. The chosen gauge described by Hamiltonian equation (1) is the so-called rung gauge [21] in which the hopping matrix elements on the legs are real and on the rungs are complex. By a unitary transformation

$$a_r = e^{-ir\frac{\phi}{2}} c_{1,r}, \quad b_r = e^{ir\frac{\phi}{2}} c_{2,r}, \tag{3}$$

one can make the hopping matrix elements on the legs complex and on the rungs real which is the so-called leg gauge [21]. The Hamiltonian H_0 is then rewritten as

$$H_{\text{leg}} = -J \sum_{r=1}^{R-1} \sum_{\ell=1}^{2} \left(e^{i\frac{\phi}{2}} a_{r+1}^\dagger a_r + e^{-i\frac{\phi}{2}} b_{r+1}^\dagger b_r + \text{H.c.} \right) - J_\perp \sum_{r=1}^{R} \left(a_r^\dagger b_r + \text{H.c.} \right). \tag{4}$$

The choice of gauge determines the distribution of the complex phases along the ladder legs or rungs. Researchers select the appropriate gauge based on the experimental schemes used to realize artificial gauge fields in quantum-engineered systems. Different setups may require different gauge choices, depending on how the effective Peierls phases are implemented [11–13, 15, 16]. The quasi-momentum distributions also depend on the gauge, reflecting characteristics specific to certain ground-state phases of the flux-ladder Hamiltonian [21, 22]. In studies involving quantum quench dynamics and quantum walks starting from localized states, the gauge choice plays a crucial role. The phase factor between the leg gauge and rung gauge operators, as shown in equation (3), introduces phase differences in the localized states constructed by local creation operators. These phase differences result in distinct dynamical behaviors under different gauge choices, which will be discussed in section 3.1.

The single-particle Hamiltonian is more easily diagonalized in the leg gauge [13, 19, 22, 23, 36]. In the momentum space, the single-body Hamiltonian H_{leg} takes the form:

$$H_{\text{leg}} = \sum_k \begin{pmatrix} a_k^\dagger & b_k^\dagger \end{pmatrix} \mathcal{H}(k) \begin{pmatrix} a_k \\ b_k \end{pmatrix}, \tag{5}$$

$$\mathcal{H}(k) = -2J \cos k \cos \frac{\phi}{2} - 2J \sin k \sin \frac{\phi}{2} \sigma_z - J_\perp \sigma_x, \tag{6}$$

where the momentum operators are introduced through the Fourier transformation of the local operator along the legs, $a_k = \frac{1}{\sqrt{R}} \sum_r e^{ikr} a_r$ and $b_k = \frac{1}{\sqrt{R}} \sum_r e^{ikr} b_r$, with quasimomenta $k = 2\pi m/R$, where m is an integer and R is the number of ladder rungs; σ_z and σ_x are Pauli matrices. The Hamiltonian is easily diagonalized through $\begin{pmatrix} \alpha_k \\ \beta_k \end{pmatrix} = \begin{pmatrix} \cos\frac{\theta_k}{2} & \sin\frac{\theta_k}{2} \\ -\sin\frac{\theta_k}{2} & \cos\frac{\theta_k}{2} \end{pmatrix} \begin{pmatrix} a_k \\ b_k \end{pmatrix}$, with $\tan\theta_k = \frac{J_\perp/J}{2\sin k \sin\frac{\phi}{2}}$, which leads the Hamiltonian to take the form $H_{\text{leg}} = \sum_k E_+(k)\alpha_k^\dagger \alpha_k + E_-(k)\beta_k^\dagger \beta_k$, where $E_\pm(k) = -2J\cos k \cos\frac{\phi}{2} \pm \sqrt{4J^2 \sin^2 k \sin^2\frac{\phi}{2} + J_\perp^2}$ describing the two bands [13, 19, 22, 23, 36]. The band structure for the parameters used in our quantum walk simulations ($\phi = 0.7\pi$, $J = 1$, $J_\perp = 2$, $R = 60$) is shown in figure 4(c). A comprehensive overview of the non-interacting system can be found in references [19, 22, 23], while discussions related to quantum walk dynamics, including those relevant to our work, can be found in references [13, 36].

2.2. Observables

The local currents are the key (experimental measurable) observables for characterizing various phases in the flux ladder [21]. In the Heisenberg equation of motion for the local particle number, we take the expectation value on both sides to obtain $\langle \frac{dn_{\ell,r}}{dt} \rangle = i\langle [H, n_{\ell,r}] \rangle$. The changing rate of the local particle number $n_{\ell,r}$ is determined by the currents flowing out from site (ℓ, r) to its neighboring sites. This gives the relation $\langle \frac{dn_{\ell,r}}{dt} \rangle = \langle j_{\ell,r}^\parallel \rangle - \langle j_{\ell,r-1}^\parallel \rangle \pm \langle j_r^\perp \rangle$, which allows us to compute current operators using the commutator $[H, n_{\ell,r}]$. Specifically, for the model described by equation (1), we define the local current operator on the legs as

$$j_{\ell,r}^\parallel = iJ\left(c_{\ell,r+1}^\dagger c_{\ell,r} - c_{\ell,r}^\dagger c_{\ell,r+1} \right), \tag{7}$$

and the current operator on the rung as

$$j_r^\perp = iJ_\perp \left(e^{-ir\phi} c_{1,r}^\dagger c_{2,r} - e^{ir\phi} c_{2,r}^\dagger c_{1,r} \right). \tag{8}$$

Another important observable is the chiral current (also dubbed edge, screening or Meissner current) defined as

$$j^c = \frac{1}{R-1} \sum_{r=1}^{R-1} \langle j_{1,r}^\parallel - j_{2,r}^\parallel \rangle, \tag{9}$$

characterizing the average current circulating the ladder along the legs.

The flux-ladder model hosts a variety of emergent quantum phases (see reference [21, 28] for comprehensive analyses), including the Meissner phase, vortex-liquid phase, vortex-lattice phase, and others. In the Meissner phase, rung currents vanish but a finite chiral current is present. In the vortex phases, rung currents emerge, and various vortex configurations can occur. The vortex-lattice phase consists of regular structures of localized vortices, whereas the vortex-liquid phase does not exhibit pinned vortices and displays irregular leg-current patterns. These three phases can exit on top of superfluid and Mott insulator, distinguished by the central charge and entanglement entropy.

Researchers typically identify vortices by examining local current configurations due to the difficulty of quantitative characterization [20, 21, 31, 32]. The complexity arises because the local leg currents are influenced by both the propagation of vortices and the circulation currents of these vortices, making it difficult to distinguish the vortices. Meanwhile, the local particle number can also fingerprint the vortices during spreading. To this end, we construct an operator to characterize a vortex by concurrently considering the local currents (both $\langle j_r^\perp \rangle$ and $\langle j_{\ell,r}^\parallel \rangle$) and particle density ($\langle n_{\ell,r} \rangle$) at the associated sites. While vortices may expand across multiple unit cells in more complex cases [31], we focus on the minimal configuration where the vortex resides within a single unit cell (plaquette) of four sites, which represents the smallest and irreducible structure. Subsequently, in analogy with classical angular momentum, a semiclassical vortex angular momentum is defined as

$$L(r) = \frac{1}{2}\langle n_{1,r} + n_{2,r} \rangle \langle j_r^\perp \rangle - \frac{1}{2}\langle n_{1,r+1} + n_{2,r+1} \rangle \langle j_{r+1}^\perp \rangle + \frac{1}{2}\langle n_{2,r} + n_{2,r+1} \rangle \langle j_{2,r}^\parallel \rangle - \frac{1}{2}\langle n_{1,r} + n_{1,r+1} \rangle \langle j_{1,r}^\parallel \rangle \tag{10}$$

to identify a vortex by neglecting correlated quantum fluctuations.

Two-particle operators are commonly employed to analyze particle correlations in studies of two-particle quantum walks in interacting systems [40–44]. The rung current correlator $\langle j_{r1}^\perp j_{r2}^\perp \rangle$ has been used to reveal important properties of the vortex phases [35]. For our aim, it is crucial to account for correlations between

particles and local currents within the vortex. We thus construct two two-particle hopping correlation operators across four lattice sites within the vortex by defining two dimeric correlators as

$$\text{DC}_1(r) = |\langle c_{1,r}c_{2,r}^\dagger c_{1,r+1}c_{2,r+1}^\dagger \rangle + \langle c_{1,r}^\dagger c_{2,r}c_{1,r+1}^\dagger c_{2,r+1} \rangle| \tag{11}$$

and

$$\text{DC}_2(r) = |\langle c_{1,r}^\dagger c_{2,r}^\dagger c_{1,r+1}c_{2,r+1} \rangle + \langle c_{1,r}c_{2,r}c_{1,r+1}^\dagger c_{2,r+1}^\dagger \rangle|, \tag{12}$$

representing correlations between pairs of neighboring dimers on the rungs and legs, respectively. They capture the correlations of hopping along these legs or rungs within a vortex, which are related to the current correlators.

To measure the delocalization, we calculated the participation ratio (PR). For each leg of the ladder, the PR is defined as $\text{PR}_\ell(t) = \sum_r |\langle \psi(t)|n_{\ell,r}|\psi(t)\rangle|^2$, where $\ell = 1,2$ denotes the two legs. The total PR is given by the sum of PRs from the two legs $\text{PR}_{\text{tot}}(t) = \text{PR}_1(t) + \text{PR}_2(t)$. Maximal localization occurs when all the particles occupy the same site, yielding $\text{PR}_{\text{tot}}(t) = N^2$, where N is the total particle number. Conversely, in the fully delocalized case where particles are equally distributed across all sites, the total PR becomes $\text{PR}_{\text{tot}}(t) = N^2/2R$, where R is the total number of rungs in the ladder. In addition to the PR, we compute the inverse PR (IPR), given by $\text{IPR}(t) = 1/\sum_r |\langle \psi(t)|\frac{n_r}{N}|\psi(t)\rangle|^2$, where $n_r = \langle n_{1,r} + n_{2,r}\rangle$ is the particle density on each rung. Maximal localization occurs when $\text{IPR}(t) = 1$, while $\text{PR}(t) = R$ represents maximally delocalization.

Furthermore, to capture the spatial dynamics of particle propagation, we also consider the MSD, defined as $\text{MSD}(t) = \sum_{\ell,r}(r - r_0)^2 P_{\ell,r}(t)$, where r_0 is the central site and $P_{\ell,r}(t)$ is the probability of the corresponding quantity localized at site (ℓ,r) at time t. The typical MSD for the classical diffusion is $\text{MSD} = 2Jt$ (take the diffusion coefficient $D = 1$ which is of the same order as J) while for a 1D single-particle quantum walk, it follows $\text{MSD} = 2(Jt)^2$ [55].

3. Results

In this section, we present and analyze the quantum walks initiated from states with one, two, and four particles localized at the central sites of the ladder. The time evolution of the quantum states under the Hamiltonian is simulated by a time-evolving block decimation (TEBD) method [56–60]. We set fixed discarded weight *cutoff* $= 10^{-8}$ and time-step $\delta = 0.1$. We start with the single-particle systems, studying the impact of choice of gauge and initial state on dynamics. Then, in two-particle systems, we discuss vortex propagation under uniform magnetic fields and on-site interaction with two different initial states. Third, we extend our research to four-particle systems, where the different types of pairing can coexist and the paired particles can interact with other particles. We provide detailed analysis by comparing the results across different conditions.

3.1. Single-particle quantum walks

First, we investigate the impact of the gauge choice and initial state construction on single-particle systems. The dynamics in quantum walks depend crucially on the initial states. We observe that the quantum walk of rung-localized single-particle initial states exhibits chiral dynamics, where the local particle propagating to the right is predominantly concentrated on one leg while to the left is concentrated on the other leg. For instance, the initial state $|\psi(0)\rangle_{1C} = \frac{1}{\sqrt{2}}(a_{30}^\dagger \pm b_{30}^\dagger)|0\rangle$ describes a single-particle state initially localized on the central rung at $r = 30$ in a ladder system of length $R = 60$. The number in the subscript of the state specifies the number of particles, distinguishing between single-, two-, and four-particle states. The subscript C indicates chiral dynamics, which have been investigated through theoretical simulations and experimental platforms [13, 36]. Instead of the rung-localized states, we consider leg-localized states. These states are superpositions of two single-particle states localized at adjacent sites in the center of the upper leg ($\ell = 2$) at $r = 30$ and $r = 31$, respectively. They are defined as $|\psi(0)\rangle_{1S} = \frac{1}{\sqrt{2}}(c_{2,30}^\dagger + c_{2,31}^\dagger)|0\rangle$ and $|\psi(0)\rangle_{1A} = \frac{1}{\sqrt{2}}(c_{2,30}^\dagger - c_{2,31}^\dagger)|0\rangle$. Here, the subscripts S and A indicate symmetric and antisymmetric superpositions, respectively.

It is worth noting that the initial states throughout this work (including the single-particle initial states $|\psi(0)\rangle_{1S}$, $|\psi(0)\rangle_{1A}$, and the two- or four-particle initial states discussed in the following subsections) are defined using the rung gauge operator $c_{\ell,l}^\dagger$. This contrasts with the leg gauge operators $a_r^\dagger$ and $b_r^\dagger$ in $|\psi(0)\rangle_{1C}$ which are generally chosen in the studies focusing on the chirality [13, 36]. These alternative initial states offer a distinct perspective on quantum walk dynamics.

Figure 2 shows the evolution of the leg current $\langle j_{\ell,r}^\parallel \rangle$ (left panel) and the local particle density $\langle n_{\ell,r}\rangle$ (right panel). The result explicitly shows that the chirality in the dynamics disappears for both initial states $|\psi(0)\rangle_{1S}$
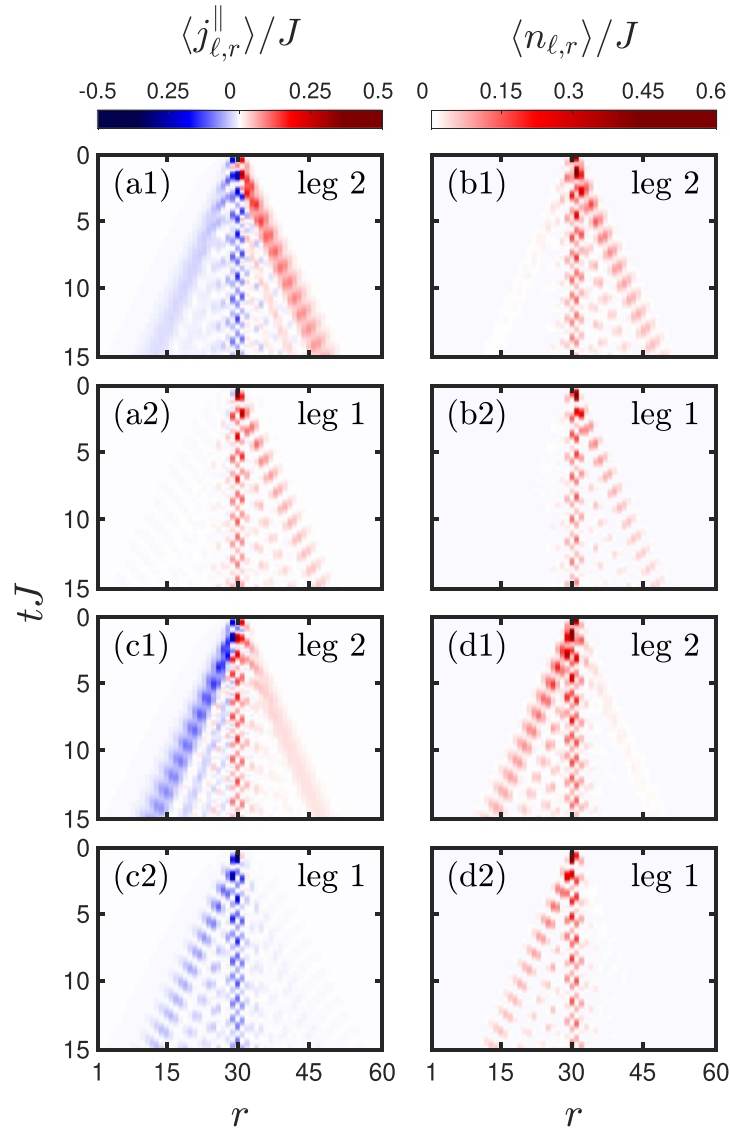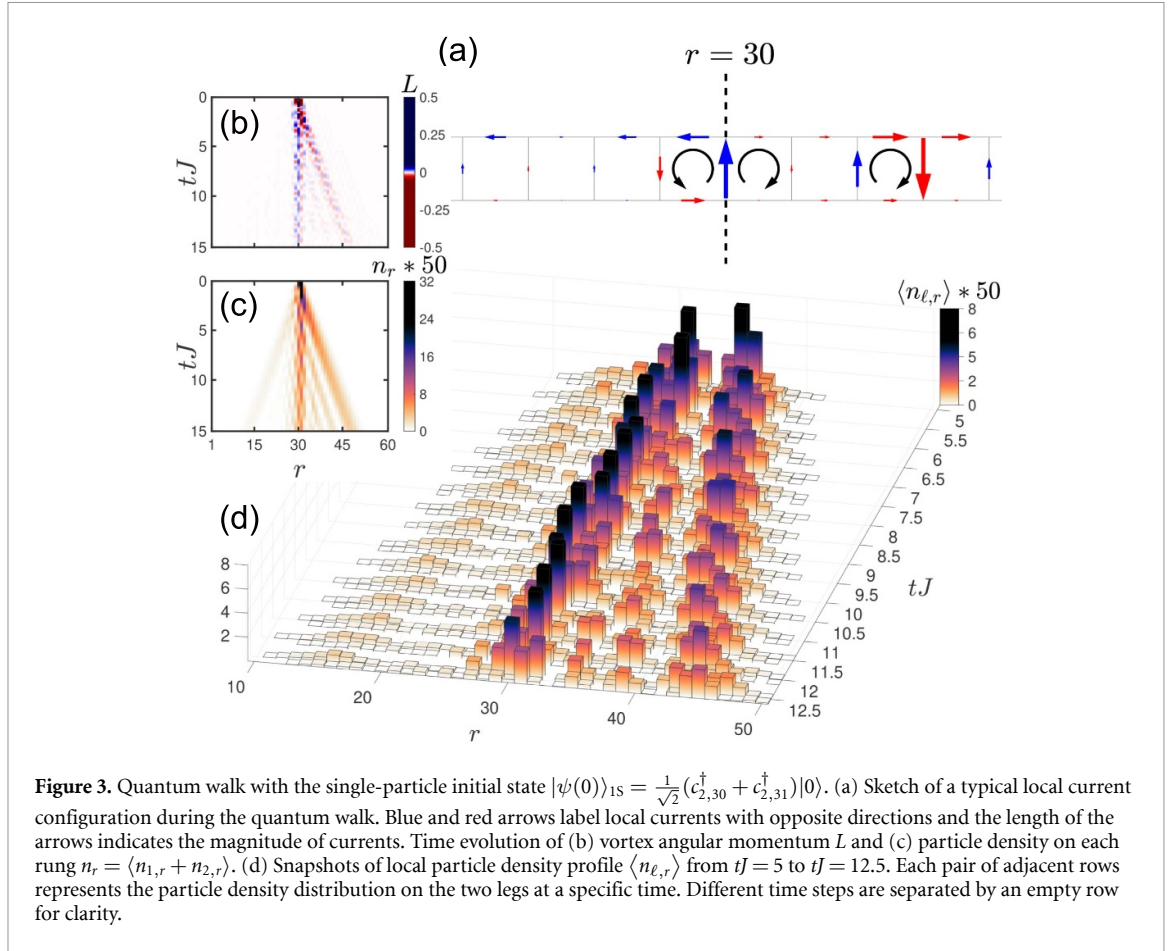
Figure 2. Time evolution of the local leg current $\langle j^{\parallel}_{\ell,r}\rangle$ (left panel) and the local particle density $\langle n_{\ell,r}\rangle$ (right panel) for the initial states: (a) and (b) $|\psi(0)\rangle_{1S} = \frac{1}{\sqrt{2}}\left(c^{\dagger}_{2,30} + c^{\dagger}_{2,31}\right)|0\rangle$; (c) and (d) $|\psi(0)\rangle_{1A} = \frac{1}{\sqrt{2}}\left(c^{\dagger}_{2,30} - c^{\dagger}_{2,31}\right)|0\rangle$.

and $|\psi(0)\rangle_{1A}$. Particularly, the spreading of currents and particles is biased toward the same directions, resulting in asymmetry. The initial state determines the direction of bias in spreading: rightward for $|\psi(0)\rangle_{1S}$ and leftward for $|\psi(0)\rangle_{1A}$. For the lower leg ($\ell = 1$) ((a2), (b2), (c2), or (d2) in figure 2), the propagations of local currents and particle density are predominantly restricted towards one-half of the ladder, resulting in their almost complete absence in the other half. Meanwhile, for the upper leg ($\ell = 2$) ((a1), (b1), (c1), or (d1) in figure 2), the majority of propagation is also towards the same half as their corresponding lower legs. However, a small component propagates to the other side.

Figure 3(a) illustrates a typical local current configuration during the quantum walk with initial state $|\psi(0)\rangle_{1S}$. The complexity arises because the local leg currents are influenced by both the group velocity of particles in propagating vortices and the circulation currents of these vortices. Consequently, the local current configurations are often messy and complicated during time evolution, making it difficult to distinguish the vortices. In figure 3(a), localized vortices near the central sites of the ladder (around $r = 30$) are easily identified, while the vortices on the right are less evident, even with a reversed lower leg current. Under these circumstances, employing operators for quantitative description becomes both efficient and essential. Figure 3(b) displays the time evolution of L for the initial state $|\psi(0)\rangle_{1S}$. There are two branches of vortices: one is localized and the other propagates to the right. In the left half of the ladder, the propagating particle mostly populates the upper leg ($\ell = 2$) (figure 2(b)), similar to the chiral spreading case [13, 36]. As a result, the lower leg currents and the rung currents vanish (figure 2(a2)), leaving only the upper leg currents

Figure 3. Quantum walk with the single-particle initial state $|\psi(0)\rangle_{1S} = \frac{1}{\sqrt{2}}(c^\dagger_{2,30} + c^\dagger_{2,31})|0\rangle$. (a) Sketch of a typical local current configuration during the quantum walk. Blue and red arrows label local currents with opposite directions and the length of the arrows indicates the magnitude of currents. Time evolution of (b) vortex angular momentum L and (c) particle density on each rung $n_r = \langle n_{1,r} + n_{2,r}\rangle$. (d) Snapshots of local particle density profile $\langle n_{\ell,r}\rangle$ from $tJ = 5$ to $tJ = 12.5$. Each pair of adjacent rows represents the particle density distribution on the two legs at a specific time. Different time steps are separated by an empty row for clarity.

(figure 2(a1)), which cannot form vortices. Figures 3(c) and (d) shows the time evolution of particle density profile, clearly demonstrating the exotic asymmetric spreading which deviates from a typical quantum walk.

We further investigate the time evolution of quasi-momentum distributions along the legs

$$n_\ell(k) = \frac{1}{R}\sum_{r,r'} e^{ik(r'-r)}\langle c^\dagger_{\ell,r}c_{\ell,r'}\rangle, \tag{13}$$

which are measurable in time-of-flight experiments [12, 61]. Using equation (3) one can relate the quasi-momentum distributions in two different gauges via linear phase shifts

$$n_1(k) = n_a(k - \phi/2), \quad n_2(k) = n_b(k + \phi/2), \tag{14}$$

where $n_a(k)$ and $n_b(k)$ are quasi-momentum distributions in the leg gauge. As noted above, the initial states $|\psi(0)\rangle_{1S} = \frac{1}{\sqrt{2}}(c^\dagger_{2,30} + c^\dagger_{2,31})|0\rangle$ and $|\psi(0)\rangle_{1A} = \frac{1}{\sqrt{2}}(c^\dagger_{2,30} - c^\dagger_{2,31})|0\rangle$ are given by means of the rung gauge operator $c^\dagger_{\ell,l}$. While the leg gauge operators $a^\dagger_r$ and $b^\dagger_r$ in $|\psi(0)\rangle_{1C} = \frac{1}{\sqrt{2}}(a^\dagger_{30} \pm b^\dagger_{30})|0\rangle$ are generally chosen in the studies focusing on the chirality [13, 36], the Hamiltonian can be easily diagonalized in the momentum space of leg gauge [19, 22–24]. For instance, with regard to initial states $\frac{1}{\sqrt{2}}(a^\dagger_{30} \pm b^\dagger_{30})|0\rangle$, particles only populate either the upper or the lower band displayed in figure 4(c). This implies particles on the two legs have opposite quasi-momenta k, resulting in chiral behaviors. However, for $|\psi(0)\rangle_{1S} = \frac{1}{\sqrt{2}}(c^\dagger_{2,30} + c^\dagger_{2,31})|0\rangle$, both the momentum distributions $n_1(k)$ and $n_2(k)$ in figure 4 are asymmetric with respect to the $k = 0$ axis as they are shifted according to equation (14). Specifically, $n_1(k)$ is predominantly concentrated on the $k < 0$ side, while $n_2(k)$ is concentrated in the range $-0.5\pi < k < 0.5\pi$, showing a weaker preference towards $k < 0$. In essence, the key factors leading to the exotic asymmetric spreading is the particular construction of superposition states $|\psi(0)\rangle_{1S}$ and $|\psi(0)\rangle_{1A}$, along with the choice of the rung gauge.
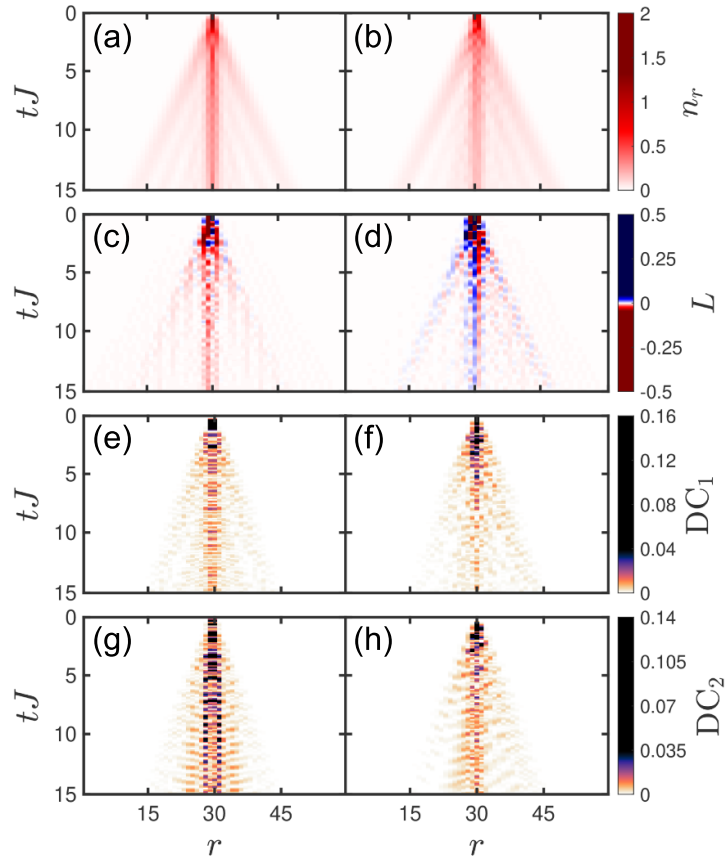
3.2. Two-particle quantum walks

In this section, we study the quantum walks with flux and on-site interaction in the two-particle systems. Similar to the single-particle initial states, we consider the initial states with two particles localized on the adjacent sites. In particular, the particles localized at the central rung $|\psi(0)\rangle_{2R} = c^\dagger_{1,30}c^\dagger_{2,30}|0\rangle$ or at the center
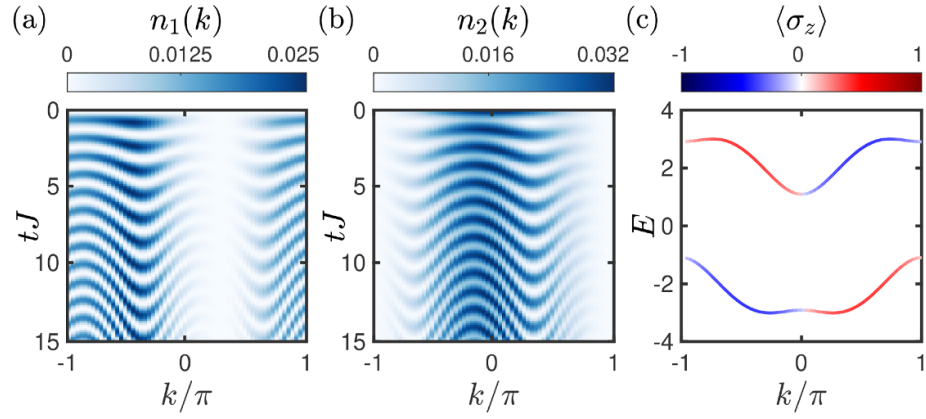
Figure 4. (a) and (b) Time evolution of momentum distribution (a) $n_1(k)$ and (b) $n_2(k)$ for the single-particle initial states $|\psi(0)\rangle_{1S} = \frac{1}{\sqrt{2}}(c^\dagger_{2,30} + c^\dagger_{2,31})|0\rangle$. (c) Energy bands of equation (5) with $\phi = 0.7\pi$, $J = 1$, $J_\perp = 2$, $U = 2$, $R = 60$. The color represents the value of $\langle\sigma_z\rangle$, where spin-up and spin-down correspond to the occupation on upper leg ($\ell = 2$) and lower leg ($\ell = 1$), respectively.
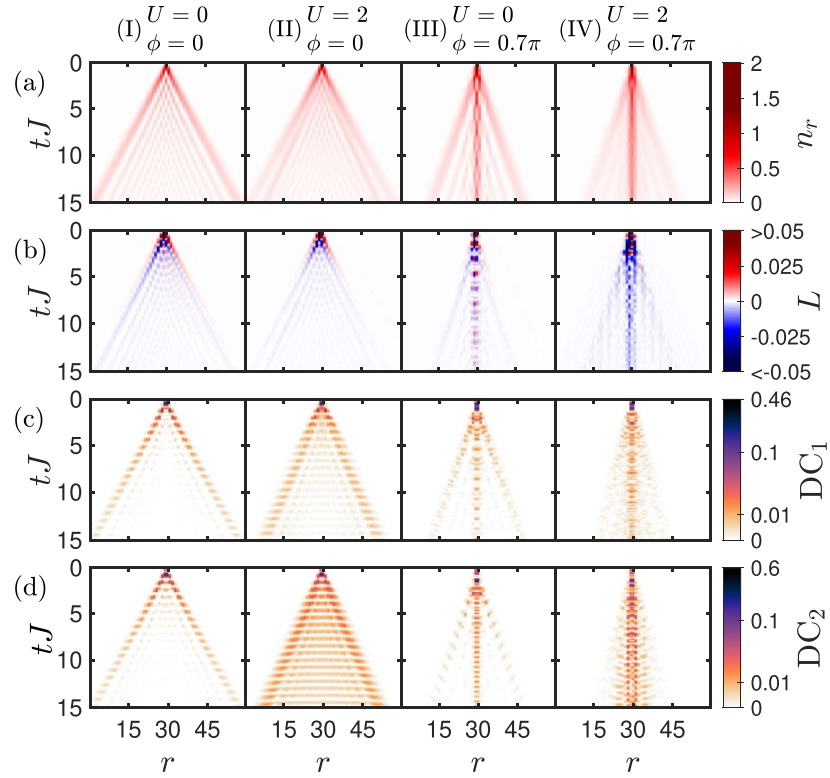

Figure 5. Quantum walks with two-particle initial states $|\psi(0)\rangle_{2R} = c^\dagger_{1,30}c^\dagger_{2,30}|0\rangle$ (left panel) and $|\psi(0)\rangle_{2L} = c^\dagger_{2,30}c^\dagger_{2,31}|0\rangle$ (right panel) with $U = 2$ and $\phi = 0.7\pi$: (a) and (b) particle density on each rung $n_r = \langle n_{1,r} + n_{2,r}\rangle$, (c) and (d) vortex angular momentum L, (e) and (f) dimeric correlator DC_1, (g) and (h) dimeric correlator DC_2.

of the upper leg $|\psi(0)\rangle_{2L} = c^\dagger_{2,30}c^\dagger_{2,31}|0\rangle$, respectively. Here, the subscript R denotes the particles localized at the same rung ($r = 30$), while the subscript L refers to the particles localized at adjacent sites on the same leg ($\ell = 2$). The subscript 2 indicates that the system contains two particles, as introduced in the previous section. The results are shown in figures 5–8.

The combined effects of uniform flux ϕ and on-site interaction U on two-particle quantum walks with the initial state $|\psi(0)\rangle_{2R}$ has been systematically studied [37]. It reveals the reentrant dynamics associated with the formation, breaking, and reformation of rung-pair states. As shown in figure 5, the results for the initial states $|\psi(0)\rangle_{2R}$ are consistent with the findings in in reference [37]. The results for $|\psi(0)\rangle_{2L}$ also exhibit similar behaviors that a substantial proportion of n_r remains localized around the central sites.
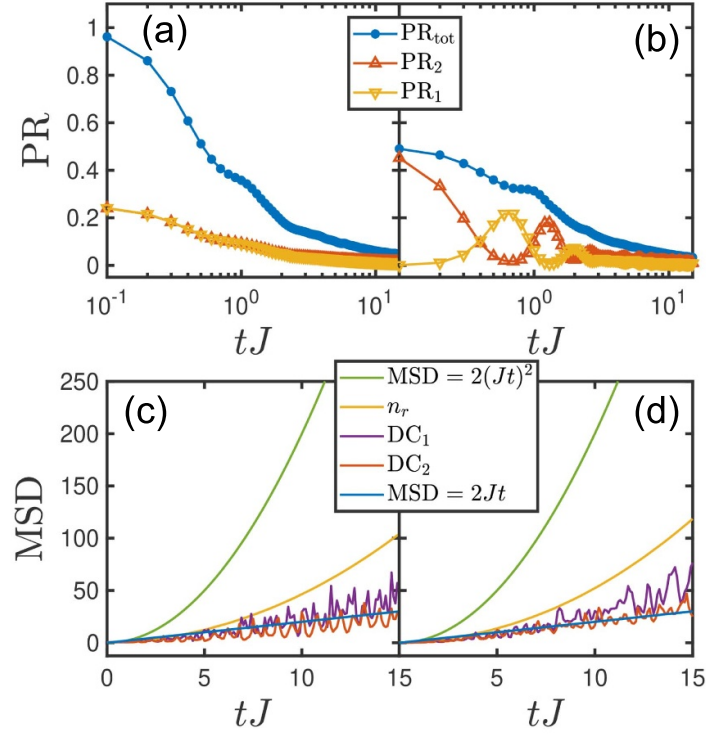
Figure 6. Quantum walks with two-particle initial states $|\psi(0)\rangle_{2R} = c_{1,30}^{\dagger} c_{2,30}^{\dagger}|0\rangle$ (left panel) and $|\psi(0)\rangle_{2L} = c_{2,30}^{\dagger} c_{2,31}^{\dagger}|0\rangle$ (right panel) with $U = 2$ and $\phi = 0.7\pi$: (a) and (b) participation ratio for the total ladder (PR_{tot}) and for each leg (PR_1 and PR_2), (c) and (d) mean square distance (MSD).

Figure 7. Quantum walks with two-particle initial state $|\psi(0)\rangle_{2R} = c_{1,30}^{\dagger} c_{2,30}^{\dagger}|0\rangle$. The columns correspond to the following parameter sets: (I) $U = 0, \phi = 0$; (II) $U = 2, \phi = 0$; (III) $U = 0, \phi = 0.7\pi$; and (IV) $U = 2, \phi = 0.7\pi$. (a) Particle density on each rung: $n_r = \langle n_{1,r} + n_{2,r}\rangle$. (b) Vortex angular momentum L. (c) and (d) Dimeric correlators $DC_1(r)$ and $DC_2(r)$. Note that the color bars for $DC_1(r)$ and $DC_2(r)$ are shown on a base-2 logarithmic scale.
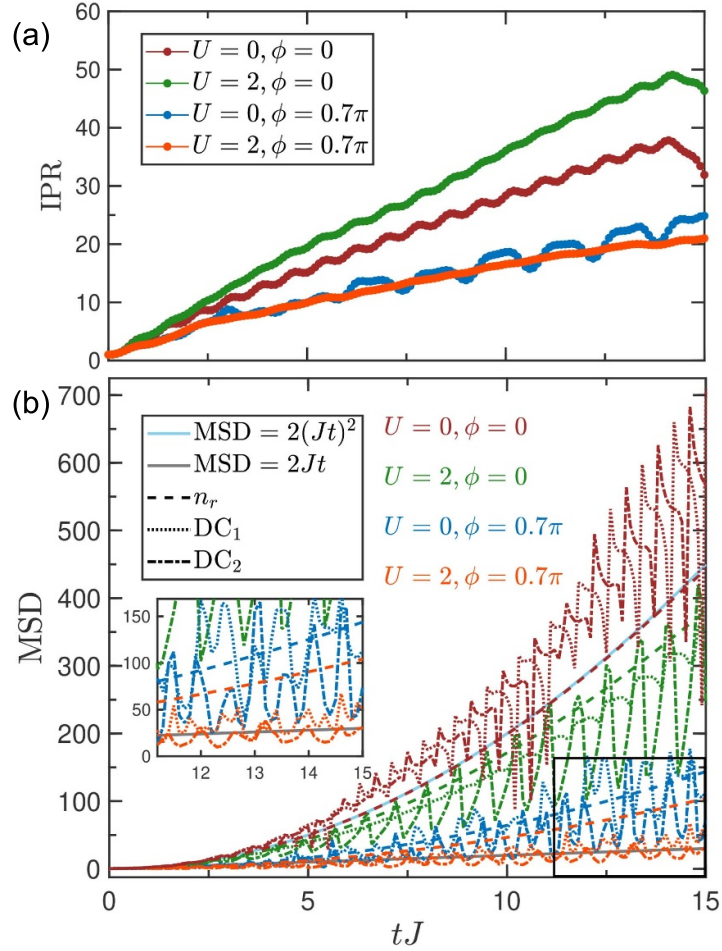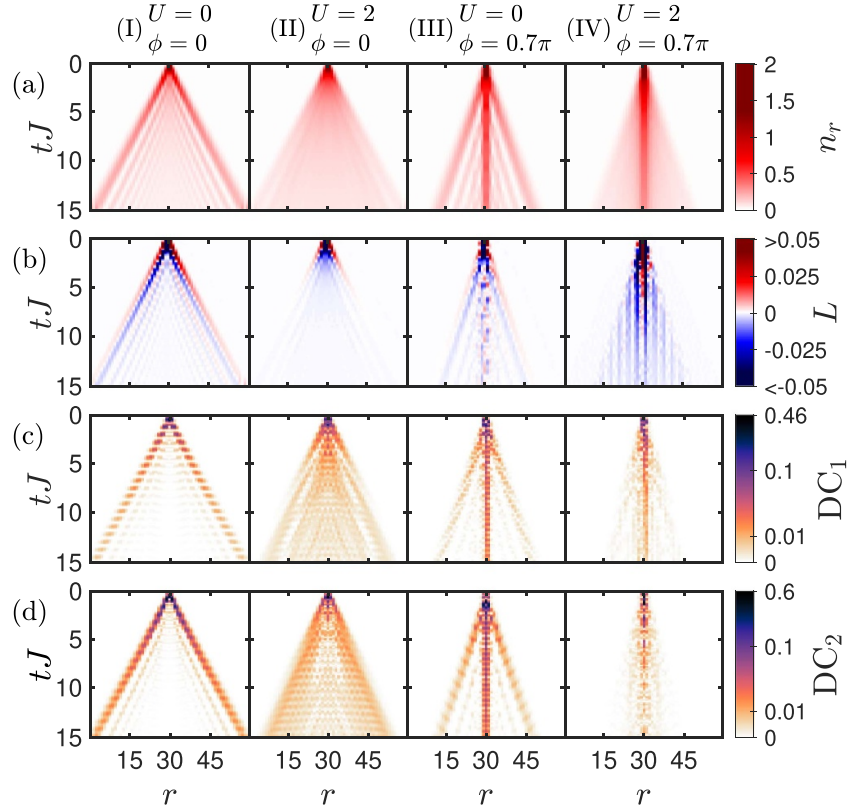
Figure 8. Quantum walks with two-particle initial state $|\psi(0)\rangle_{2R} = c_{1,30}^{\dagger}c_{2,30}^{\dagger}|0\rangle$: (a) inverse participation rate (IPR), (b) mean square distance.

Similarly, significant proportions of L, DC_1 and DC_2 are concentrated near the central region, signaling that the localized particles form vortices oscillating within the central region. In our systems, the formation of boson pairs give rise to the two-particle dynamics that coexist with the single-particle dynamics [37]. Consequently, both paired and single particles propagate outwards, contributing to the distributions of DC_1 and DC_2 beyond the central region.

To measure the delocalization, we calculate the PR of each leg in figures 6(a) and (b). The PR decreases rapidly and then slows down to saturate for both initial states. However, for $|\psi(0)\rangle_{2L}$ (figure 6(b)), the PR of $\langle n_{1,r}\rangle$ and $\langle n_{2,r}\rangle$ exhibit an alternating oscillation, indicating the particles initially localized on the same leg oscillating coherently between the two legs during the propagation. This two-particle dynamics is absent for $|\psi(0)\rangle_{2R}$, presumably because the pairing type favored by $|\psi(0)\rangle_{2L}$ differs from the rung-pair observed in $|\psi(0)\rangle_{2R}$.

Figures 6(c) and (d) shows MSD. For comparison, we plotted the MSD for the classical diffusion $MSD = 2Jt$ (take the diffusion coefficient $D = 1$ which is of the same order as J) and the 1D single-particle quantum walk $MSD = 2(Jt)^2$ [55]. Notably, the MSD of DC_1 and DC_2 for both two-particle states aligns with classical diffusion but with sharp fluctuations, indicating that the vortex propagates classically. A more detailed analysis of this transition will be provided following the discussion of the four-particle quantum walk results.

In figures 7 and 8, we present the quantum walks across different conditions with the initial states $|\psi(0)\rangle_{2R} = c_{1,30}^{\dagger}c_{2,30}^{\dagger}|0\rangle$. As shown in the second column of figure 7 with $U = 2, \phi = 0$, the particle pair induced by the interaction exhibits an effective single-particle behavior, leading to the emergence of a narrower cone within the density distribution [42]. In the third column of figure 7 with $U = 0, \phi = 0.7\pi$, the introduction of flux induces the formation of vortices. The oscillation of localized vortices around the central sites and the ballistic propagation of other vortices can be observed in the density distribution. These results in figures 7 and 8 show similarities to the four-particle system, therefore more detailed discussions are deferred to the subsequent subsection on four-particle quantum walks.

Figure 9. Quantum walks with four-particle initial state $|\psi(0)\rangle_4 = c^\dagger_{1,30}c^\dagger_{2,30}c^\dagger_{1,31}c^\dagger_{2,31}|0\rangle$. The columns correspond to the following parameter sets: (I) $U = 0, \phi = 0$; (II) $U = 2, \phi = 0$; (III) $U = 0, \phi = 0.7\pi$; and (IV) $U = 2, \phi = 0.7\pi$. (a) Particle density on each rung: $n_r = \langle n_{1,r} + n_{2,r} \rangle$. (b) Vortex angular momentum L. (c) and (d) Dimeric correlators $DC_1(r)$ and $DC_2(r)$. Note that the color bars for $DC_1(r)$ and $DC_2(r)$ are shown on a base-2 logarithmic scale.

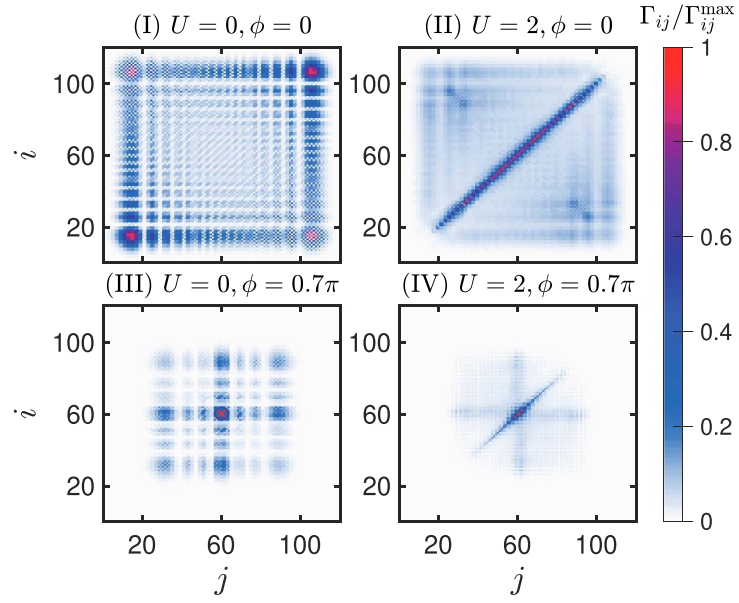### 3.3. Four-particle quantum walks

In this section, we mainly investigate multi-particle dynamics focusing on the motion of vortices under fixed flux and on-site interaction. We consider the initial state $|\psi(0)\rangle_4 = c^\dagger_{1,30}c^\dagger_{2,30}c^\dagger_{1,31}c^\dagger_{2,31}|0\rangle$, corresponding to four particles created at the central plaquette of the ladder ($\ell = 1, 2; r = 30, 31$), with one particle at each site. The subscript 4 indicates the system contains four particles, consistent with the previous sections. In this configuration, different types of pairing induced by on-site interactions can coexist. Figure 9 shows the time evolution of n_r, L, DC_1 and DC_1 under four different conditions. The corresponding density-density correlation function

$$\Gamma_{ij} = \langle c^\dagger_i c^\dagger_j c_i c_j \rangle, \tag{15}$$

are shown in figure 10, where i and j are the site index of the ladder. The index i (or j) is defined with the rung index r and leg index ℓ as $i = 2(r - 1) + \ell$.

When the flux and interaction are absent, as shown in the first column of figure 9 with $U = 0, \phi = 0$, the particles spread across the lattice independently. The coherent interference of all single-particle paths leads to ballistic transport with a well-defined wavefront, exhibiting the characteristic density distribution of a single-particle quantum walk. In this regime, bosons bunch in the propagating wavefront, making the vortex angular momentum (L) and dimeric correlators ($DC_1(r)$ and $DC_2(r)$) prominent within the wavefront.

Upon switching on the interactions, as shown in the second column of figure 9 with $U = 2, \phi = 0$, the fragmentation of the density distribution vanishes, transitioning into a uniform cone shape. The significant correlations along the diagonals of Γ_{ij} in the second column of figure 10 are signatures of pairing, suggesting that the particles propagating outwards as a composite unit of multiple particles, and the paired particles can still interact with the other particles. Consequently, the dimeric correlators ($DC_1(r)$ and $DC_2(r)$) emerge in the central region and become more uniformly distributed. This is one of the situations where the two-particle quantum walks deviate significantly from the four-particle quantum walks. In the two-particle quantum walks as shown in figure 7, the pair has not got additional particles to form interactions. As a result, the particle pair exhibits an effective single-particle behavior, leading to less uniform particle density distributions compared to the four-particle systems.

Figure 10. Quantum walks with the four-particle systems with initial state $|\psi(0)\rangle_4 = c^\dagger_{1,30}c^\dagger_{2,30}c^\dagger_{1,31}c^\dagger_{2,31}|0\rangle$. The density-density correlation function $\Gamma_{ij} = \langle c^\dagger_i c^\dagger_j c_i c_j \rangle$ at $tJ = 12.5$ for (I) $U = 0, \phi = 0$, (II) $U = 2, \phi = 0$, (III) $U = 0, \phi = 0.7\pi$, and (IV) $U = 2, \phi = 0.7\pi$. The relationship between i (or j) and the rung index r and leg index ℓ is defined as $i = 2(r-1) + \ell$.

The introduction of flux significantly impacts the behavior of propagating particles. Free particles, which exhibit ballistic spreading above, begin to circulate upon the application of flux, leading to the formation of vortices. Specifically, as shown in the third column of figure 9 with $U = 0, \phi = 0.7\pi$, some particles become localized around the initial sites, while others continue their outward ballistic propagation, albeit becoming slower after the introduction of flux. In the third column of figure 10, the localized particles exhibit strong correlations, indicating the formation of vortices and their oscillation around the central sites. The absence of diagonal elements in the correlation matrix suggests the particle pairings are absent, while the finite off-diagonal elements arise from the single-particle dynamics, which are slowed down by the flux. This behavior is consistent with the findings in reference [37] that the ballistic spreading slows down as the flux ϕ increases from 0 to π for $U = 0$. The vortex angular momentum (L) and dimeric correlators ($DC_1(r)$ and $DC_2(r)$) patterns remain prominent within the wavefronts of ballistic propagation, with additional central localized vortices making them distinct at the central sites.

Unusual reentrant behaviors have been observed in the quantum walk of interacting bosons on a flux ladder arising from the competition between the interaction strength U and the applied flux, which influences the formation of particle pairs [37]. As shown in the fourth column of figure 9 with $U = 2, \phi = 0.7\pi$, the particle pairings induced by interaction U lead to a more uniform density distribution, while notable localization around the central sites caused by the applied flux persists. The emergence of a vertical fringe pattern in the vortex angular momentum L (figure 9(b)), which is less pronounced in two-particle systems(figure 7(b)), reveals the formation of periodically spaced vortices within the flux ladder [21, 37]. We conjecture that these vortices move outward step by step, maintaining fixed periodic spacing in the expanding region. Although this behavior suggests structured vortex dynamics, a more detailed investigation is required to clarify the precise movement of individual vortices during this hopping process. However, the dimeric correlators ($DC_1(r)$ and $DC_2(r)$) do not exhibit the same vertical fringe patterns as L, possibly overshadowed by contributions from the propagation of paired particles.

The IPR shown in figures 11(a). Initially, the IPR increases linearly in all cases. At later times, the IPR for $U = 0, \phi = 0$ decreases as the ballistically spreading particles reach the boundary, whereas the IPR for $U = 2, \phi = 0$ saturates near the maximal delocalization value. Notably, the introduction of interaction increases the particle delocalization for $\phi = 0$, but this effect is not evident for $\phi = 0.7\pi$.

Figure 11(b) shows MSD. Our results indicate that the individual application of flux and interaction slows down the particle propagation as the MSD of n_r becomes significantly smaller than that of the single-particle quantum walk. Most interestingly, when both flux and interaction are present together ($U = 2, \phi = 0.7\pi$), the MSD of DC_1 and DC_2 fits well with classical diffusion, indicating the vortices propagate in a classical manner. The discussions regarding IPR and MSD also apply to the two-particle system, although figure 8 shows greater fluctuations for both IPR and MSD.
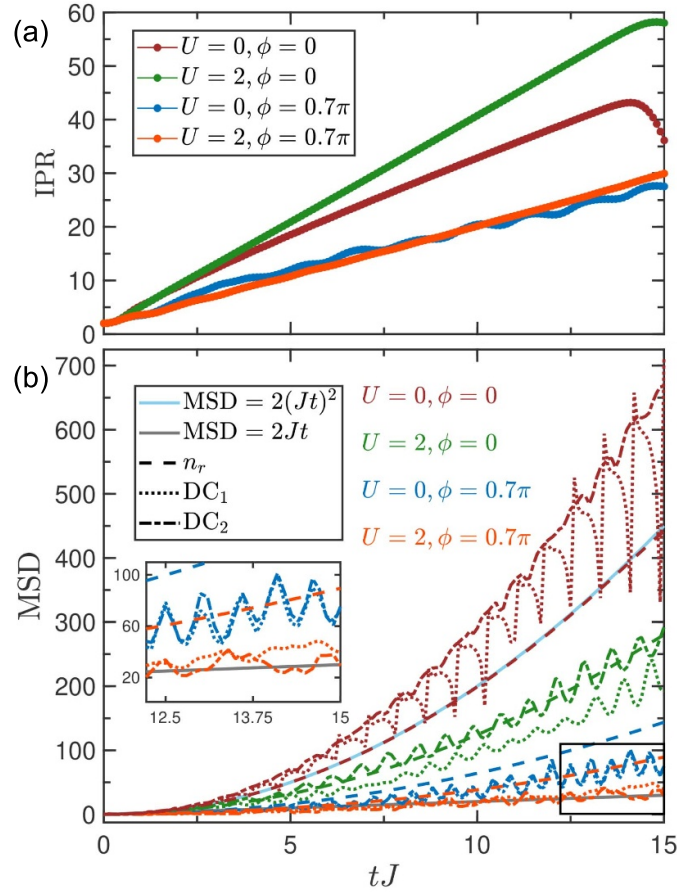
Figure 11. Quantum walks with four-particle initial state $|\psi(0)\rangle_4 = c_{1,30}^{\dagger} c_{2,30}^{\dagger} c_{1,31}^{\dagger} c_{2,31}^{\dagger} |0\rangle$: (a) inverse participation rate (IPR), (b) mean square distance.

It is known that the decoherence and disorder can lead to classical diffusive behavior in 1D systems [48, 49]. In our observations, the transition to classical diffusion of vortex propagation, analogous to vortex creep in superconductors, occurs without the need dephasing terms in this quantum lattice system, demonstrating that the interplay between flux and interaction alone can induce classical vortex behavior within this purely quantum-mechanical framework. Furthermore, for quantum walks on a 2D square lattice with flux, the spreading may exhibit classical diffusive behaviors, with a significant probability of finding the walker at the origin [47]. In our ladder system, which serves as a transitional case between 1D and 2D systems, we observe that the MSD for the case of $U = 0, \phi = 0.7\pi$ approaches classical diffusion (MSD = $2Jt$) but remains above it, indicating that the transition to classical diffusion is not complete in the individual application of flux. Moreover, the further application of interaction contributes to the transition that the MSD fits well with the classical diffusion in the case of $U = 2, \phi = 0.7\pi$ where vortices exhibit classical behavior.

4. Conclusion

In summary, we simulated the quantum walks of classical vortex creep in a lattice model, specifically focusing on quantum walks initiated from states with one, two, and four particles in an interacting bosonic flux ladder. By introducing the vortex angular momentum and the dimeric operators, we explored the effective characterization of the vortex in a quantum lattice model framework. Notably, the dimeric operator may prove useful in future investigations of dimer models, as it can quantify correlations between different dimer configurations of the ground state.

In the single-particle systems, we observed the exotic asymmetry, where the propagation is strongly biased toward one end of the ladder. This asymmetry arises from the specific construction of the initial states and the choice of the rung gauge. In the two- and four-particle systems, we observed the emergence of particle pairing upon introducing interactions, leading to composite multi-particle dynamics. Under the influence of magnetic fields, particles that initially exhibited ballistic transport began to circulate and form

vortices, slowing their propagation. When both flux and interaction are present simultaneously, the MSD of these vortices fits adequately well with classical diffusion, indicating that these vortices propagate classically. This classical vortex behavior emerges purely from the interplay between flux and interaction within a quantum framework.

Our observations can be experimentally realized with present quantum technologies. Especially, similar quantum walks on the flux-ladder model have been investigated in an experiment using cold atoms in optical lattices [13]. Our exploration contributes to the understanding of the classical-quantum correspondence of vortices, presenting an innovative way to investigate the vortex behaviors. Further extension of our work to explore the effects of defects and temperature on vortex behavior is expected, which could inform the development of advanced superconducting applications.

Data availability statement

The data that support the findings of this study are available upon reasonable request from the authors.

Acknowledgment

ORCID iD

Weijie Huang ⬤ https://orcid.org/0000-0003-1881-4099

References

[1] Brandt E H 1995 *Rep. Prog. Phys.* **58** 1465
[2] Kwok W-K, Welp U, Glatz A, Koshelev A E, Kihlstrom K J and Crabtree G W 2016 *Rep. Prog. Phys.* **79** 116501
[3] Foltyn S, Civale L, MacManus-Driscoll J, Jia Q, Maiorov B, Wang H and Maley M 2007 *Nat. Mater.* **6** 631
[4] Blatter G, Feigel'man M V, Geshkenbein V B, Larkin A I and Vinokur V M 1994 *Rev. Mod. Phys.* **66** 1125
[5] Blatter G, Geshkenbein V B and Vinokur V M 1991 *Phys. Rev. Lett.* **66** 3297
[6] Gorokhov D A, Fisher D S and Blatter G 2002 *Phys. Rev.* B **66** 214203
[7] Mota A, Juri G, Pollini A, Aupke K, Teruzzi T, Visani P and Hilti B 1992 *Phys. Scr.* **1992** 69
[8] Eley S, Miura M, Maiorov B and Civale L 2017 *Nat. Mater.* **16** 409
[9] Buchacek M, Willa R, Geshkenbein V B and Blatter G 2019 *Phys. Rev.* B **100** 014501
[10] Cole H M, Venuti M B, Gorman B, Bauer E D, Chan M K and Eley S 2023 *Phys. Rev.* B **107** 104509
[11] Atala M, Aidelsburger M, Lohse M, Barreiro J T, Paredes B and Bloch I 2014 *Nat. Phys.* **10** 588
[12] Stuhl B K, Lu H-I, Aycock L M, Genkina D and Spielman I B 2015 *Science* **349** 1514
[13] Tai M E, Lukin A, Rispoli M, Schittko R, Menke T, Borgnia D, Preiss P M, Grusdt F, Kaufman A M and Greiner M 2017 *Nature* **546** 519
[14] Ye Y *et al* 2019 *Phys. Rev. Lett.* **123** 050502
[15] Li Y, Du H, Wang Y, Liang J, Xiao L, Yi W, Ma J and Jia S 2023 *Nat. Commun.* **14** 7560
[16] Wang Y, Wu Y-K, Jiang Y, Cai M-L, Li B-W, Mei Q-X, Qi B-X, Zhou Z-C and Duan L-M 2024 *Phys. Rev. Lett.* **132** 130601
[17] Orignac E and Giamarchi T 2001 *Phys. Rev.* B **64** 144515
[18] Petrescu A and Le Hur K 2013 *Phys. Rev. Lett.* **111** 150601
[19] Wei R and Mueller E J 2014 *Phys. Rev.* A **89** 063617
[20] Piraud M, Heidrich-Meisner F, McCulloch I P, Greschner S, Vekua T and Schollwöck U 2015 *Phys. Rev.* B **91** 140406
[21] Greschner S, Piraud M, Heidrich-Meisner F, McCulloch I P, Schollwöck U and Vekua T 2016 *Phys. Rev.* A **94** 063628
[22] Hügel D and Paredes B 2014 *Phys. Rev.* A **89** 023619
[23] Tokuno A and Georges A 2014 *New J. Phys.* **16** 073005
[24] Keleş A and Oktel M O 2015 *Phys. Rev.* A **91** 013629
[25] Buser M, Heidrich-Meisner F and Schollwöck U 2019 *Phys. Rev.* A **99** 053601
[26] Çeven K, Oktel M O and Keleş A 2022 *Phys. Rev.* A **106** 063320
[27] Yu J, Sun N and Zhai H 2017 *Phys. Rev. Lett.* **119** 225302
[28] Buser M, Hubig C, Schollwöck U, Tarruell L and Heidrich-Meisner F 2020 *Phys. Rev.* A **102** 053314
[29] Dhar A, Mishra T, Maji M, Pai R V, Mukerjee S and Paramekanti A 2013 *Phys. Rev.* B **87** 174501
[30] Di Dio M, De Palo S, Orignac E, Citro R and Chiofalo M-L 2015 *Phys. Rev.* B **92** 060506
[31] Greschner S, Piraud M, Heidrich-Meisner F, McCulloch I P, Schollwöck U and Vekua T 2015 *Phys. Rev. Lett.* **115** 190402
[32] Greschner S and Vekua T 2017 *Phys. Rev. Lett.* **119** 073401
[33] Petrescu A and Le Hur K 2015 *Phys. Rev.* B **91** 054520
[34] Song Y-F and Yang S-J 2020 *New J. Phys.* **22** 073001
[35] Chen J-D, Tu H-H, Wu Y-H and Xu Z-F 2020 *Phys. Rev.* A **102** 043322
[36] Guan X, Feng Y, Xue Z-Y, Chen G and Jia S 2020 *Phys. Rev.* A **102** 032610
[37] Giri M K, Paul B and Mishra T 2023 *Phys. Rev.* A **108** 063319
[38] Giri M K, Paul B and Mishra T 2024 *Phys. Rev.* A **109** 043308
[39] Li S-S, Ge Z-Y and Fan H 2020 *Phys. Rev.* A **102** 062409
[40] Lahini Y, Verbin M, Huber S D, Bromberg Y, Pugatch R and Silberberg Y 2012 *Phys. Rev.* A **86** 011603
[41] Preiss P M, Ma R, Tai M E, Lukin A, Rispoli M, Zupancic P, Lahini Y, Islam R and Greiner M 2015 *Science* **347** 1229

[42] Wiater D, Sowiński T and Zakrzewski J 2017 *Phys. Rev. A* **96** 043629
[43] Qin X, Ke Y, Guan X, Li Z, Andrei N and Lee C 2014 *Phys. Rev. A* **90** 062301
[44] Yan Z *et al* 2019 *Science* **364** 753
[45] An F A, Meier E J and Gadway B 2018 *Phys. Rev. X* **8** 031045
[46] Márquez-Martín I, Arnault P, Di Molfetta G and Pérez A 2018 *Phys. Rev. A* **98** 032333
[47] Yalçınkaya İ and Gedik Z 2015 *Phys. Rev. A* **92** 042324
[48] Chandrashekar C M 2011 *Phys. Rev. A* **83** 022320
[49] Schreiber A, Cassemiro K N, Potoček V, Gábris A, Jex I and Silberhorn C 2011 *Phys. Rev. Lett.* **106** 180403
[50] Razzoli L, Paris M G A and Bordone P 2020 *Phys. Rev. A* **101** 032336
[51] Sajid M, Asbóth J K, Meschede D, Werner R F and Alberti A 2019 *Phys. Rev. B* **99** 214303
[52] Troisi A and Orlandi G 2006 *Phys. Rev. Lett.* **96** 086601
[53] Cheung D L and Troisi A 2008 *Phys. Chem. Chem. Phys.* **10** 5941
[54] McMahon D P and Troisi A 2010 *Chem. Phys. Chem.* **11** 2067
[55] Hartmann T, Keck F, Korsch H J and Mossmann S 2004 *New J. Phys.* **6** 2
[56] White S R 1992 *Phys. Rev. Lett.* **69** 2863
[57] Schollwöck U 2005 *Rev. Mod. Phys.* **77** 259
[58] Schollwöck U 2011 *Ann. Phys., NY* **326** 96
[59] Fishman M, White S R and Stoudenmire E M 2022 *SciPost Phys. Codebases* (https://doi.org/10.21468/SciPostPhysCodeb.4)
[60] Fishman M, White S R and Stoudenmire E M 2022 Codebase release 0.3 for ITensor *SciPost Phys. Codebases* 4-r0.3
[61] Celi A, Massignan P, Ruseckas J, Goldman N, Spielman I B, Juzeliūnas G and Lewenstein M 2014 *Phys. Rev. Lett.* **112** 043001